A Parallel Numerical Method for Risk Assessment of Myocardial Infarction during Liver Transplantation: a Case Study

Zhengzheng Yan[1], Dandan Shang[2], Jingzhi Li[3,*] and Rongliang Chen[1,*]

[1] *Shenzhen Institutes of Advanced Technology, Chinese Academy of Sciences, Shenzhen, Guangdong 518055, China*
[2] *Department of Cardiology, Shenzhen Second People's Hospital, the First Affiliated Hospital of Shenzhen University, Shenzhen, Guangdong 518035, China*
[3] *Department of Mathematics, Southern University of Science and Technology, Shenzhen, Guangdong 518055, China*

Abstract. Coronary artery disease is a devastating complication of some patients undergoing liver transplantation. Anesthesia, anhepatic blood flow occlusion, and reperfusion of the liver can cause severe fluctuations in hemodynamics. However, the vast majority of liver transplant patients cannot undergo invasive coronary examinations due to their critical illness and abnormal coagulation function. In this paper, we present a retrospective case of acute myocardial infarction during surgery in order to demonstrate a noninvasive method to obtain coronary hemodynamic functional information based on scalable computational fluid dynamics technology. A $P_1 - P_1$ stabilized finite element method and second-order backward differentiation formula are applied to discretize the time-dependent Navier-Stokes equations in the spatial and temporal directions, respectively. A Windkessel model constructed based on the measured clinic data is used to characterize the outlet blood flow. We then apply a parallel Newton-Krylov method with a restricted additive Schwarz preconditioner to accelerate the timeliness of the simulation. The simulated functional indicator successfully verifies the myocardial ischemia in the anhepatic phase of liver transplantation. We also present the parallel performance of the algorithm on a supercomputer, and the results show that the proposed solver achieves over 55% parallel efficiency with 3840 processor cores.

---

*Corresponding author.
Emails: zz.yan@siat.ac.cn (Z. Yan), dandan.shang@gmail.com (D. Shang), li.jz@sustech.edu.cn (J. Li), rl.chen@siat.ac.cn (R. Chen)

1   Introduction

Coronary artery disease (CAD) is one of the most worrisome complications of liver transplantation (LT) surgery and carries high morbidity and mortality [1]. Studies have revealed that cardiovascular events remain a leading cause of early mortality (40%), followed by infection (28%) and graft failure (12%) [2]. LT is a high-risk surgery, and underlying CAD is considered a relative contraindication to the procedure [3]. LT is a significant cardiovascular stressor, as surgical operations such as intraoperative anesthesia, clamping of the hepatic vein and reperfusion can result in abnormal cardiovascular hemodynamic behavior. Myocardial ischemia or myocardial infarction (MI) will occur when the blood flow to the myocardium is affected and is insufficient during surgery. Accordingly, a thorough, accurate and rapid risk assessment of perioperative myocardial ischemia and further therapeutic intervention are essential for LT patients.

Currently, there is no consensus or standardized guideline regarding CAD risk assessment in the pretransplant period [4]. Each institution uses its own protocol, such as electrocardiography, ultrasonography, stress tests or nuclear myocardial perfusion imaging, for CAD risk assessment, and the final decision depends on the individual characteristics, with widespread variation in practice across LT centers [5]. Nevertheless, noninvasive coronary computed tomography angiography (CCTA) examination is recommended by some guidelines [6,7] to evaluate the CAD risk. CCTA is an anatomic test and provides an expeditious and cost-effective method of assessing patients at intermediate risk for CAD, that is, anatomically obstructive CAD ($\leq 50\%$ luminal narrowing). However, perioperative myocardial infarction is also observed in LT patients with nonobstructive coronary artery stenosis [8]. Some studies have reported that anatomical stenosis does not directly result in functional ischemia [9,10].

Since myocardial infarction is caused by an insufficient blood supply to the myocardium, that is, changes in coronary hemodynamics, cardiologists have developed an interventional technique, i.e., fractional flow reserve (FFR) [11], to assess the risk of CAD from the hemodynamic function perspective. FFR is defined as the ratio of maximum flow in the presence of stenosis to the normal maximum flow [12]. Clinically, FFR is a blood pressure ratio measured by a sensor on the tip of a guidewire during hyperemia by injecting adenosine or papaverine. The guidelines suggest that FFR≤ 0.8 indicates myocardial ischemia, and revascularization surgery (such as stenting) is needed to improve the patient's myocardial blood supply. However, in addition to the need for contrast and tolerating the radiation used to guide the operation, we need to put a pressure wire into the coronary arteries to measure their pressures. LT patients are usually in critical condition and have abnormal coagulation function, and most patients cannot undergo invasive coronary FFR examination. Therefore, although the invasive FFR has become the gold-standard method for risk assessment of myocardial ischemia, it is unrealistic to use it to preoperatively assess the risk of CAD for patients planning to undergo LT.

In the past few years, novel technologies that utilize computational fluid dynamics [13–17] and conventional medical imaging data have made significant progress in

obtaining the FFR noninvasively. Representatively, computed tomography (CT)-derived fractional flow reserve (FFR_{CT}) [18] has demonstrated high diagnostic performance and high discriminatory power [19]. Despite limitations, e.g., dependence on quality imaging data and stable CAD requirements, the of use of FFR_{CT} proved that this emerging numerical tool is able to provide a functional perioperative myocardial ischemia evaluation of CAD by applying 3D anatomic and microvascular resistance models. Therefore, considering the need to identify high CAD risk candidates in the LT pretransplant period and the lack of any adequate methods to do so, this work shows a pilot study comparing cardiac hemodynamics occurring while undergoing CCTA and LT. The indicators of myocardial ischemia, FFR, at different surgical stages are calculated numerically for comparative analysis with clinical characteristics. Concerning the issues of timeliness, we present a domain decomposition method-based scalable solver to simulate blood flow in curved and complicated coronary artery trees.

A retrospective case of myocardial infarction in the perioperative period of LT was studied, and the preoperative CCTA examination showed that the patient had nonobstructive coronary artery stenosis. We first rebuilt the patient-specific morphological domain based on the CCTA images and then constructed boundary conditions according to the monitored blood pressure and heart rate at different stages of LT. A stabilized finite element $P_1 - P_1$ scheme on an unstructured tetrahedral mesh and a fully implicit second-order backward differentiation formula are applied for spatial and temporal discretization, respectively. A Newton-Krylov-Schwarz algorithm is applied to solve the discretized large-scale nonlinear system. Through numerical experiments, we present the calculated myocardial ischemia indicators, as well as the complex pulsatile blood flow field in tortuous cardiac arteries at each stage. Moreover, we report the parallel performance of the proposed solver carried out on a supercomputer.

The rest of the paper is organized as follows. In Section 2, we describe the details of the computational method. Section 3 is devoted discussing the retrospective case and some observations. Finally, we draw some conclusions in Section 4.

2 Methodology

2.1 Morphological domain construction

The patient-specific morphological domain is the premise of the numerical simulation of hemodynamics. The cardiovascular arteries mainly include the aortic sinus connected to the left ventricle, aorta and coronary artery. In this paper, the 3D geometry of artery trees (diameter ≥ 0.8mm) is reconstructed based on high-resolution multislice CCTA images at the end of diastole [20], as shown in Fig. 1. The relevant parameters of the CCTA images are 0.75mm slice thickness, 0.35mm pixel size, 512×512 image resolution and a total of 255 slices. The reconstructed anatomic model was evaluated by cardiovascular ultrasound data and experienced physicians to ensure an accurate geometry.

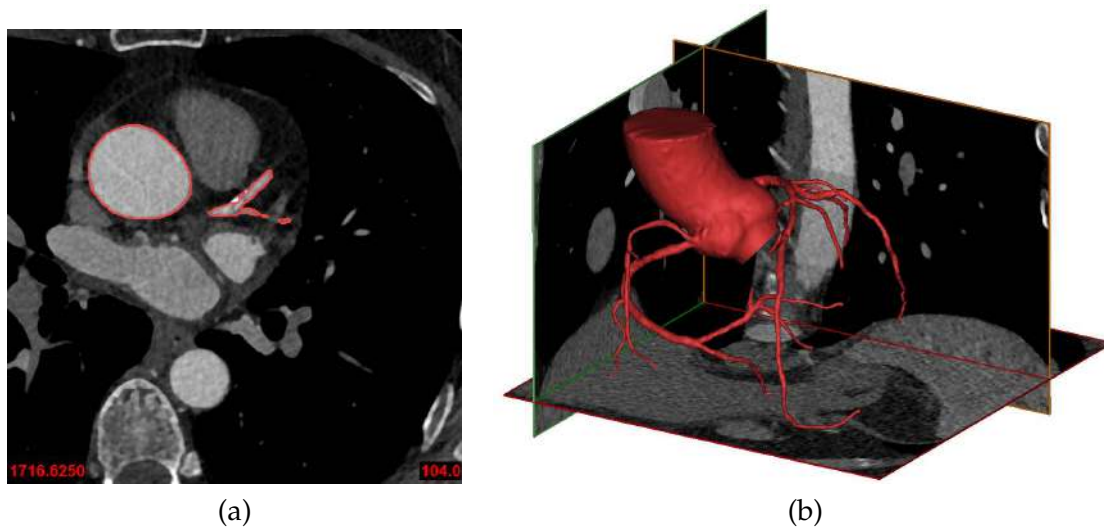(a)   (b)

Figure 1: Reconstructed patient-specific anatomical cardiovascular model (b) based on CCTA images ((a): axial view).

2.2   Governing equation and boundary condition

In this work, the blood flow is assumed to be a Newtonian incompressible fluid with constant and uniform density, $\rho = 1.050 \text{g/cm}^3$ and viscosity $\mu = 0.035 \text{cm}^2/\text{s}$. The pulsatile pumping of the heart during the cardiac cycle makes the flow unsteady, and the governing equation can be described by the following Navier-Stokes equations:

$$\frac{\partial \mathbf{u}}{\partial t} + \mathbf{u} \cdot \nabla \mathbf{u} - \nabla \cdot \sigma = \mathbf{0} \qquad \text{in } \Omega, \tag{2.1a}$$

$$\nabla \cdot \mathbf{u} = 0 \qquad \text{in } \Omega, \tag{2.1b}$$

where $\mathbf{u}$ is the blood velocity vector, $\sigma = -p\mathbf{I} + \mu(\nabla \mathbf{u} + (\nabla \mathbf{u})^T)$ is the Cauchy stress tensor, $\mathbf{I}$ is an 3×3 identity matrix, and p is the blood pressure. $\Omega \in R^3$ is the computational domain bounded by artery walls. Under the rigid wall assumption, a nonslip boundary condition is applied on the artery wall Γ_W,

$$\mathbf{u} = 0 \quad \text{on } \Gamma_W. \tag{2.2}$$

Each distinct stage of LT has its own hemodynamic characteristics, such as changes in cardiac output, heart rate, and systemic vascular resistance [21]. The hemodynamics of blood flow in the coronary artery at each stage of LT can be simulated by changing the boundary conditions based on the physiological parameters measured during the operation. However, some clinical data are destined to be unavailable with current medical device technology, and some valuable and obtainable data are not perfect enough be-

cause this case is retrospective. Therefore, we used both the measured clinical data and data from literatures to construct suitable boundary conditions.

For the cardiovascular system, the blood is pumped by the heart from the left ventricle and passes to the myocardium and other organs and tissues throughout the body. The inlet is located at the junction of the left ventricle and the aorta, which is the largest artery in the body. Cardiovascular ultrasound provides a mean blood velocity $\bar{v}_{aorta}$ in the aorta over a cardiac cycle, and combined with a recommended cardiovascular blood waveform in the literature [22], a transient velocity $\mathbf{g}$ is obtained, which is imposed on the inlet boundary Γ_I:

$$\mathbf{u} = \mathbf{g} \quad \text{on } \Gamma_I. \tag{2.3}$$

A Windkessel model [23] is imposed on the outlet boundary Γ_O. Specifically, at time t, the time-varying blood pressure $p(t)$ on the k-th artery outlet,

$$p^k(t) = [p^k(0) - R^k Q^k(0) - p_d^k(0)]e^{-\frac{t}{\tau^k}} + p_d^k(t)$$
$$+ R^k Q^k + \int_0^t \left(\frac{e^{-(t-s)/\tau}}{C^k} \right) Q^k(s) ds, \tag{2.4a}$$

where R^k is the resistance, and Q^k is the volume flow rate through the k-th outlet. p_d is the downstream pressure. $\tau^k = R_d^k C^k$ and C^k is the capacitance which is used to characterize the deformation of arteries. R^k and C^k are calculated by the rule for a parallel circuit and the area of the corresponding outlet [24],

$$R^k = R_{total} \frac{\sum (d^k)^3}{(d^k)^3}, \qquad k = 1, \cdots, n, \tag{2.5a}$$

$$C^k = C_{total} \frac{A_O^k}{\sum A_O^k}, \qquad k = 1, \cdots, n, \tag{2.5b}$$

where d_k and A_O are the diameter and area of the k-th artery outlet, respectively. R_{total} and C_{total} are the total resistance and capacitance of all artery outlets, respectively. R_{total} is calculated in the way $R_{total} = \alpha \frac{P_b}{Q_c}$, where P_b is the mean brachial pressure, α is an empirical constant, and Q_c is the flow in the coronary arteries. At each stage of LT, P_b is estimated based on the measured systolic blood pressure (SBP) and diastolic blood pressure (DBP) by empirical formulas [25]. Since studies have reported that the total blood flow delivered to the myocardium by the coronary artery is proportional to the cardiac output, here, we set Q_c equal to 4% of the inlet flow [26]. Let $\mathbf{n}$ be the outward unit surface normal to the k-th outlet Γ_O^k; then, Q^k is calculated by

$$Q^k = \int_{\Gamma_O^k} \mathbf{u}(t) \cdot \mathbf{n} d\Gamma. \tag{2.6}$$

Therefore, the outlet boundary condition (2.4) gives a relationship of the flow velocity and pressure.

2.3 Discrtization

A stabilized $P_1 - P_1$ finite element method is applied to discretize the governing equations Eq. (2.1) in the spatial domain. Define the trial and weighting function spaces as:

$$\mathcal{V} = \{ \mathbf{u} \in [H^1(\Omega)]^3 : \mathbf{u} = \mathbf{g} \text{ on } \Gamma_I, \ \mathbf{u} = \mathbf{0} \text{ on } \Gamma_W \}, \tag{2.7a}$$

$$\mathcal{V}_0 = \{ \Phi \in [H^1(\Omega)]^3 : \Phi = \mathbf{0} \text{ on } \Gamma_I \cup \Gamma_W \}, \tag{2.7b}$$

$$\mathcal{P} = L^2(\Omega). \tag{2.7c}$$

The Galerkin weak form can be written as follows: finding $\mathbf{u} \in \mathcal{V}$ and $p \in \mathcal{P}$ such that $\forall \Phi \in \mathcal{V}_0$ and $\forall q \in \mathcal{P}$:

$$B(\{\mathbf{u}, p\}, \{\Phi, q\}) = 0, \tag{2.8}$$

with

$$B(\{\mathbf{u}, p\}, \{\Phi, q\}) \equiv \rho \int_\Omega \frac{\partial \mathbf{u}}{\partial t} \cdot \Phi d\Omega + \mu \int_\Omega \nabla \mathbf{u} : \nabla \Phi d\Omega + \rho \int_\Omega (\mathbf{u} \cdot \nabla) \mathbf{u} \cdot \Phi d\Omega$$
$$- \int_\Omega p \nabla \cdot \Phi d\Omega + \int_\Omega (\nabla \cdot \mathbf{u}) p d\Omega - \int_{\Gamma_O} \tau \cdot \Phi d\Gamma, \tag{2.9}$$

where $\tau = -p\mathbf{n} + \mu(\nabla \mathbf{u} \cdot \mathbf{n})$.

The finite element pair $P_1 - P_1$ is unstable to discretize incompressible Navier-Stokes equations [27] because it does not satisfy the LBB condition. A stabilization term introduced in [28] is employed in this paper to stabilize the $P_1 - P_1$ method. On an unstructured tetrahedral mesh $\mathcal{T}^h = \{K\}$, the finite dimensional weak form is defined as follows: Finding $\mathbf{u}^h \in \mathcal{V}^h$ and $p^h \in \mathcal{P}^h$, such that $\forall \Phi^h \in \mathcal{V}_0^h$ and $\forall q^h \in \mathcal{P}^h$,

$$\bar{B}(\{\mathbf{u}^h, p^h\}, \{\Phi^h, q^h\}) = 0, \tag{2.10}$$

with

$$\bar{B}(\{\mathbf{u}^h, p^h\}, \{\Phi^h, q^h\}) \equiv B(\{\mathbf{u}^h, p^h\}, \{\Phi^h, q^h\}) + \sum_{K \in \mathcal{T}^h} \left(\nabla \cdot \mathbf{u}^h, \tau_c \nabla \cdot \Phi^h \right)_K$$
$$+ \sum_{K \in \mathcal{T}^h} \left(\mathcal{L}^h, \tau_m \left(\mathbf{u}^h \cdot \nabla \Phi^h + \nabla q^h \right) \right)_K + \sum_{K \in \mathcal{T}^h} \left(\bar{\mathbf{u}}^h \cdot \nabla \mathbf{u}^h, \Phi^h \right)_K$$
$$+ \sum_{K \in \mathcal{T}^h} \left(\bar{\mathbf{u}}^h \cdot \nabla \mathbf{u}^h, \tau_b \bar{\mathbf{u}}^h \cdot \nabla \Phi^h \right)_K, \tag{2.11}$$

where τ_c, τ_m and τ_b are the stabilization parameters. $\bar{\mathbf{u}}^h = -\tau_m \mathcal{L}^h$ and $\mathcal{L}^h$ is computed by

$$\mathcal{L}^h = \rho \frac{\partial \mathbf{u}^h}{\partial t} + \rho \mathbf{u}^h \cdot \nabla \mathbf{u}^h + \nabla p^h - \rho \mathbf{f}^h.$$

The stabilization parameters τ_m, τ_c and τ_b are defined as follows:

$$\tau_m = \left(\sqrt{\frac{4}{\Delta t^2} + (\mathbf{u}_n^h \cdot \mathbf{G} \mathbf{u}_n^h) + 36 \left(\frac{\mu}{\rho} \right)^2 G:G} \right)^{-1},$$

$$\tau_c = (8\tau_m trace(\mathbf{G}))^{-1},$$

$$\tau_d = \sqrt{\mathbf{u}_n^h \cdot \mathbf{G} \bar{\mathbf{u}}_n^h},$$

where

$$\mathbf{G} = \{G_{ij}\} = \left\{ \sum_{k=1}^{3} \frac{\partial \xi_k}{\partial x_i} \frac{\partial \xi_k}{\partial x_j} \right\}$$

is the covariant metric tensor and $\frac{\partial \xi}{\partial x}$ denotes the inverse Jacobian of the mapping between the reference and the physical element. $\mathbf{u}_n^h$ and $\bar{\mathbf{u}}_n^h$ are the counterparts of $\mathbf{u}^h$ and $\bar{\mathbf{u}}^h$ at the nth time step, respectively. Δt is the timestep size for the temporal discretization.

We rewrite Eq. (2.10) in the following simplified form to introduce the temporal discretization,

$$\frac{\mathbf{X}}{dt} = \mathbf{L}(\mathbf{X}), \tag{2.12}$$

where $\mathbf{L}(\mathbf{X})$ is the semidiscretized system of the Navier-Stokes equations, except the first term $\frac{\partial \bar{\mathbf{u}}}{\partial t}$ after spatial discretization. $\mathbf{X}$ is the vector consisting of the nodal values of the velocity and pressure. A second-order backward differentiation formula (BDF2) [29, 30] is applied for the temporal discretization of Eq. (2.12), as shown in Eq. (2.13),

$$1.5\mathbf{X}^n - 2\mathbf{X}^{n-1} + 0.5\mathbf{X}^{n-2} = \Delta t \mathbf{L}(\mathbf{X}^n). \tag{2.13}$$

Note that, in (2.13), we need two previous timestep solutions to calculate the current timestep solution. With a given initial condition $\mathbf{X}^0$, we first calculate $\mathbf{X}^1$ by the backward Euler method with time step size $0.5\Delta t$, and then step forward by (2.13) with $\mathbf{X}^0$ and $\mathbf{X}^1$.

2.4 Domain decomposition method based solver

After discretization, a large, sparse, and nonlinear system must be solved at each time step to obtain the solution at the next time step, which is simply denoted as:

$$\mathbf{F}^n(\mathbf{X}^n) = \mathbf{0}. \tag{2.14}$$

We propose a solution strategy for solving the system (2.14) based on a Newton-Krylov-Schwarz (NKS) method [31]. The NKS method is suitable for solving large, sparse nonlinear systems and has been widely applied in various problems [32, 33]. At the nth time step, let $\mathbf{X}_0^n = \mathbf{X}^{n-1}$ be the initial guess and $\mathbf{X}^n$ be the current approximate solution. The

inexact Newton's method solves the nonlinear equation system iteratively by inexactly solving a series of linearized systems

$$\mathbf{J}_k^n \mathbf{d}_k^n = -\mathbf{F}^n(\mathbf{x}_k^n),\tag{2.15}$$

to obtain the search direction $\mathbf{d}_k^n$ and then update the solution in the way

$$\mathbf{X}_{k+1}^n = \mathbf{X}_k^n + \lambda_k^n \mathbf{d}_k^n,\tag{2.16}$$

where λ_k^n is the step length obtained by a cubic backtracking line search and $\mathbf{J}_k^n$ is the Jacobian of $\mathbf{F}^n$ evaluated at $\mathbf{x}_k^n$. The system (2.15) is a large and ill-conditioned linear system, and a preconditioned GMRES method with an RAS preconditioner $\mathbf{M}_n^k$ is used to solve it inexactly such that

$$\|\mathbf{F}(\mathbf{X}_k^n) + \mathbf{J}_k^n (\mathbf{M}_n^k)^{-1} \mathbf{M}_n^k \mathbf{d}_k^n\| \le \eta_k \|\mathbf{F}(\mathbf{X}_k^n)\|,\tag{2.17}$$

where η_k is the relative tolerance to control the accuracy of the solution of the linear system.

The restricted additive Schwarz (RAS) method is an overlapping domain decomposition method [34] that starts with partitioning the computational domain Ω into n_p non-overlapping subdomains Ω_i, $i=1,\cdots,n_p$, where n_p is equal to the number of processors in this paper. Then, the overlapping subdomains Ω_i^δ are obtained by extending δ layers of elements from the neighboring subdomains, where δ represents the overlapping level. An example of the partition is shown in Fig. 2, where the computational domain, in which the number of tetrahedral elements is approximately 2.0×10^5, is decomposed into 8 subdomains and assigned to 8 processors for parallel solving. Note that since the partition is related to the load balancing in subsequent parallel computing, the number of degrees of freedom (DOFs) in each subdomain needs to be close to guarantee the parallel performance of the algorithm. The RAS preconditioner is defined as the summation of the subdomain preconditioners such that

$$(\mathbf{M}_n^k)^{-1} = \sum_{i=1}^{n_p} (R_i^0)^T (\mathbf{B}_n^k)_i^{-1} R_i^\delta,$$

where R_i^0 and R_i^δ are restriction operators from the global domain Ω to the non-overlapping subdomain Ω_i and overlapping subdomain Ω_i^δ, respectively. $(\mathbf{B}_n^k)_i^{-1}$ is a subdomain preconditioner for the subdomain Jacobian matrix $(\mathbf{J}_n^k)_i$, and it is computed approximately by point-block ILU factorization.

2.5 Hardware and software

The original CCTA images are derived from a high-resolution CT scanner (SOMATOM Force, SIEMENS), and the cardiovascular arteries are reconstructed by Mimics software (V21.0, Materialise, Ann Arbor, MI, USA) and subsequent manual surface smoothing
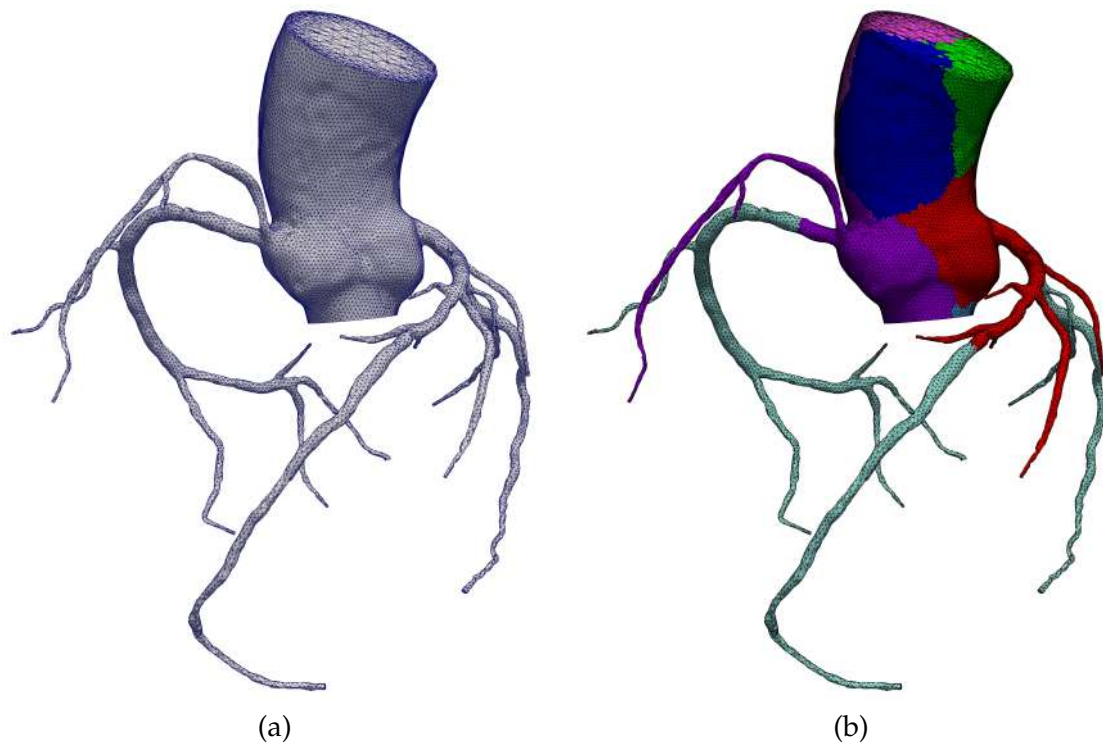
Figure 2: Schematic view of the computational mesh (a) and domain decomposition (b) for parallel computing. Each color refers to one subdomain.

processes. The solver is implemented on the top of an open source package PETSc [35]. ANSYS ICEMCFD [36] and ParMETIS [37] are employed for mesh generation and partitioning, respectively. Numerical experiments are carried out on the TianHe-2A supercomputer at China's National Supercomputing Center in Guangzhou. ParaView [38] is used for visualization of the flow field.

3 Numerical experiments and discussion

In this section, we show the numerical results of the experiment that we conducted to investigate the FFR changes due to the LT operation and the parallel scalability of the proposed solver.

This retrospective case is a patient with chronic liver failure who needed to undergo a liver transplant. Routine CCTA was examined before surgery to assess the cardiovascular risk. The CCTA images show that there are several mild stenoses at the proximal and middle of the left anterior descending (LAD) artery and the proximal right coronary artery (RCA) due to multiple spotty calcifications. After assessment of the CCTA diagno-

Table 1: Heart rate, systolic blood pressure (SBP) and diastolic blood pressure (DBP) measured in the brachial artery during the CCTA scan, anesthesia MHR and anhepatic phase. The unit of the heart rate is beats per minute (BPM), and the unit of pressure is mmHg.

Stage	Heart Rate	SBP	DBP	Cardiac Cycle (s)	T (s)	Δt (s)
CCTA Scan	80	124	58	0.75	3.00	0.075
Anesthesia MHR	95	135	75	0.63	2.52	0.063
Anhepatic Phase	90	60	40	0.67	2.68	0.067

sis, the doctors decided that the patient had a low risk of CAD. Echocardiography shows that the mean velocity of blood flow at the aorta $\bar{v}_{aorta} = 100$mm/s.

After CCTA examination, the patient underwent liver transplant surgery, and the heart rate, SBP and DBP were measured during the surgery. Table 1 shows the three sets of monitoring data, heart rate, SBP and DBP, corresponding to the CCTA examination stage, the moment of the maximum heart rate (MHR) during anesthesia, and the anhepatic phase (liver replacement, portal vein and hepatic artery from closure to opening). The patient received urgent treatment because of experiencing a sudden myocardial infarction during the anhepatic phase. We want to use the proposed method to confirm the myocardial infarction.

The inflow rate Q_{in} is calculated using the mean velocity of the blood flow at the aorta $\bar{v}_{aorta}$ and the heart rate. We assume that the stroke volume (the volume of blood pumped from the left ventricle per heart beat) is constant at all stages. Therefore, the profile of Q_{in} changes with the change in heart rate at each stage, as shown in Fig. 3. For each stage, the simulation runs for four consecutive cardiac cycles. The total simulation time T of each stage is dependent on the heart rate. The time step size is set to $\Delta t = 1/(Heart\,Rate)$.
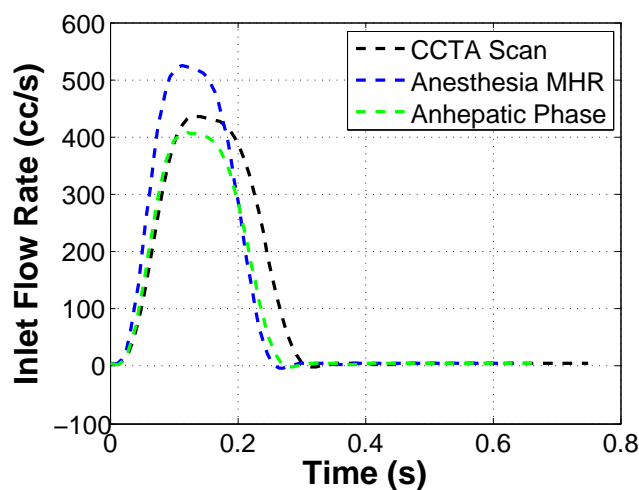

Figure 3: The time-varying inflow rate in a cardiac cycle at each stage of LT.

3.1 Fractional flow reserve calculation

The FFR is a time-averaged value over one or multiple cardiac cycles and is calculated by using the pressure distal to the stenosis P_d and the aortic pressure P_a as follows: $FFR = P_d / P_a$. Clinically, the FFR is measured at the three major branches: the left anterior descending (LAD) coronary artery, the left circumflex (LCX) coronary artery, and the right coronary artery (RCA). The percutaneous coronary intervention (PCI) guidelines suggest that patients are at high risk of myocardial ischemia and should undergo myocardial revascularization if $FFR < 0.8$ [39]. In our numerical simulation, four monitoring points ($P_1 \sim P_4$) were placed to observe the pressure and FFR. The point P_1 is at the entrance of the coronary artery, which is used to obtain the proximal pressure P_a, and $P_2 \sim P_4$, which are used to obtain the distal pressure P_d, are at the distal end of the LAD, LCX and RCA, respectively. The reconstructed vessel geometry shows that there are several mild stenoses caused by calcifications in the LAD and RCA, and we therefore refine the meshes near the lesions to better capture the flow pattern, as shown in Fig. 4.

We simulate the blood flow on two different grids M_1 and M_2 for each stage, and the maximum mesh size on the wall for these two grids is set to 0.4mm and 0.2mm, respectively. Correspondingly, the numbers of tetrahedron cells are approximately $M_1:6.99 \times 10^6$ and $M_2:1.47 \times 10^7$, and the numbers of degrees of freedom (DOFs) are approximately $M_1:5.81 \times 10^6$ and $M_2:1.22 \times 10^7$, respectively.

Unless otherwise specified, the parameters of the solver in the numerical experiments
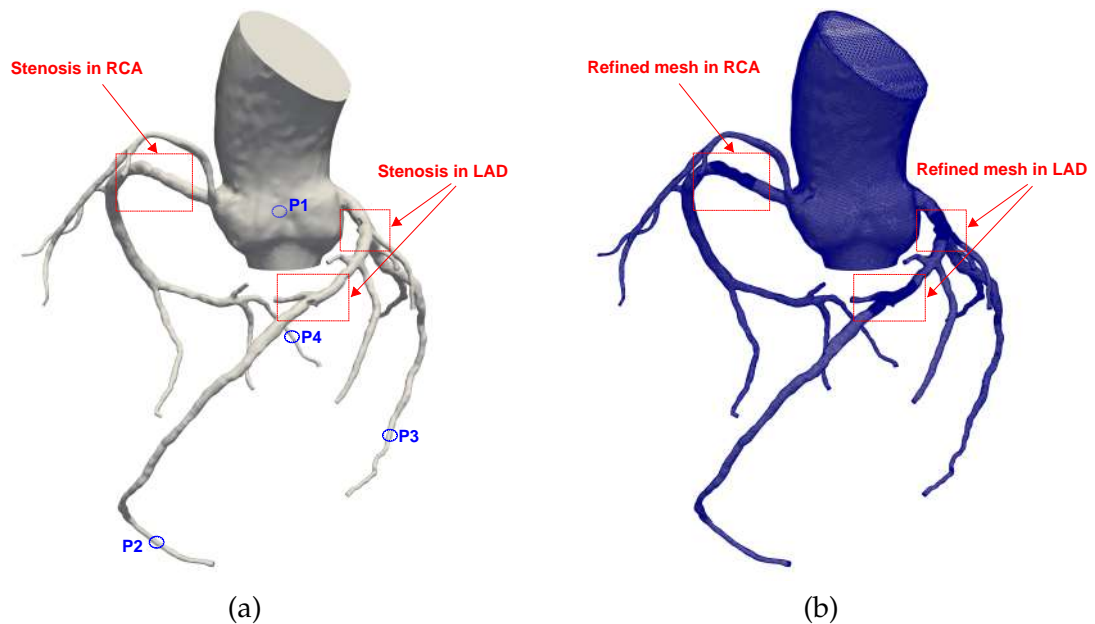

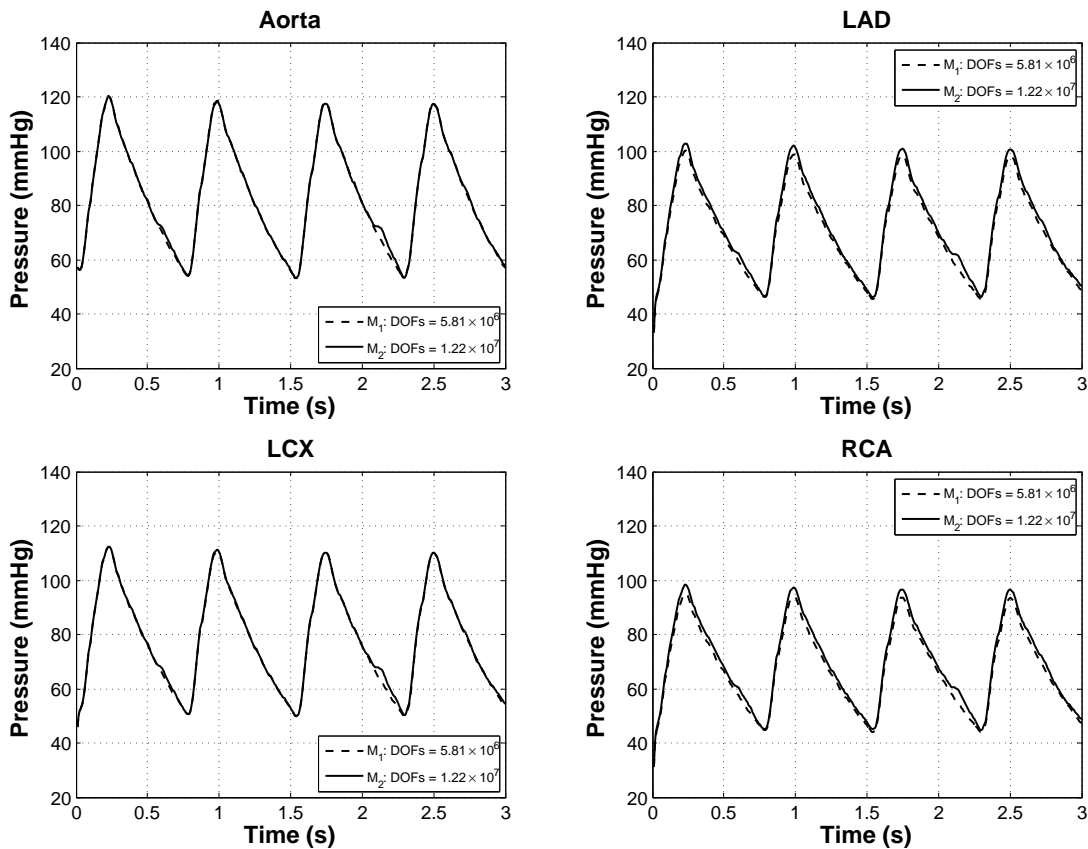Figure 4: Positions of monitoring points and computational mesh.

Figure 5: The pressure comparison with M_1 and M_2 at the four monitoring points.

are set to the overlapping size $\delta = 1$ and the level of ILU fill-ins $\ell = 1$. The restarted iteration $k = 400$ in the restart GMRES(k) algorithm. The relative tolerances of the nonlinear iteration and the linear iteration in the Newton step are set to 1.0×10^{-6} and 1.0×10^{-4}, respectively.

The pressure curves at aorta, LAD coronary artery, LCX coronary artery and RCA are presented in Fig. 5. With different mesh resolutions, M_1 and M_2, the pressure values at the peaks slightly deviate. Nevertheless, the comparison illustrates that the pressure history with the coarse mesh M_1 is almost the same as that of the fine mesh M_2, which means that the pressure almost reaches the mesh convergence on M_2.

We next put the pressure values at different stages together to analysis. Corresponding to the measured brachial artery mean pressure in Table 1, as shown in Fig. 6, at the monitoring points on the four coronary artery branches, the pressure at different stages of the CCTA scan and anesthesia MHR are a little higher than those in the anhepatic phase. The pressure waveforms presented at different stages are slightly different, which may
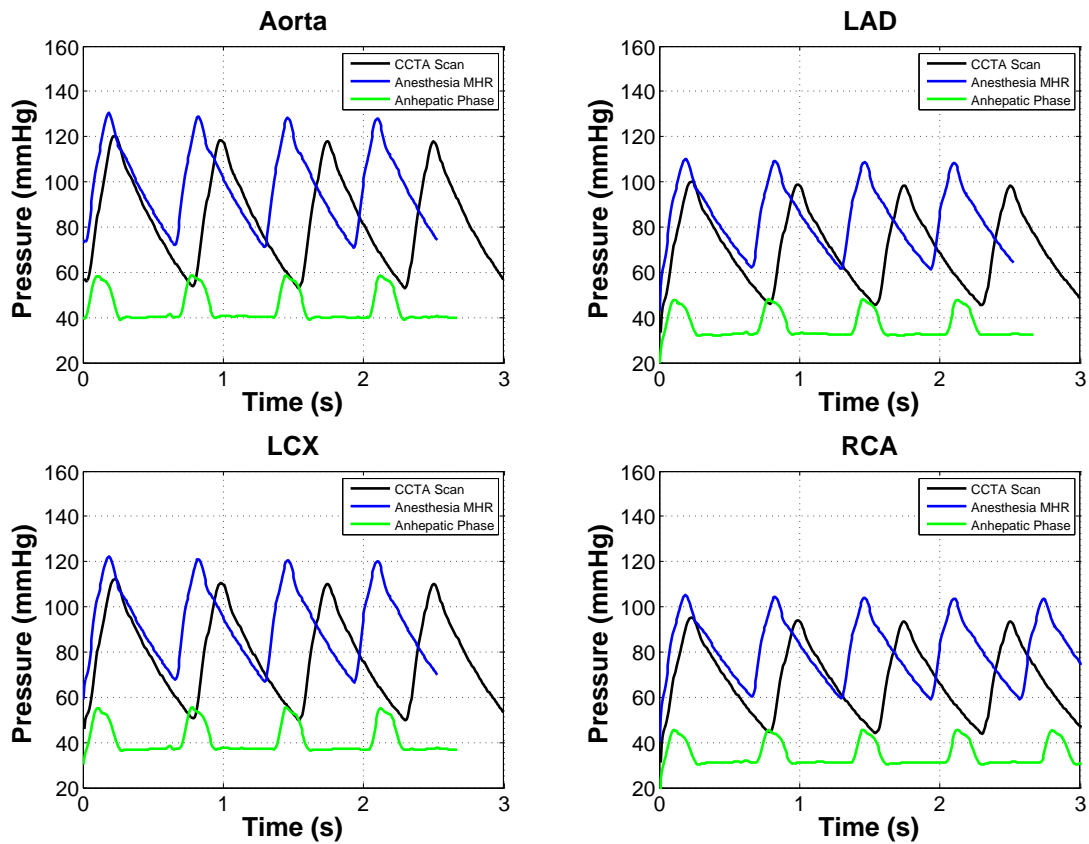
Figure 6: Pressure history at the four monitoring points under different stages of the liver transplant procedure (Aorta, LAD, LCX and RCA correspond to $P_1 \sim P_4$, respectively).

be due to the different cardiac cycle and outlet boundary conditions. Compared with those of the LAD coronary artery and RCA, the peak values and time-averaged values of the LCX pressure in all the three stages are relatively higher than the other arteries.

Table 2 and Fig. 7 present the simulated FFR of the three major branches of the coronary arteries at each stage of the operation. We have the following observations: (1) At the CCTA scan stage, although mild stenosis causes the FFR of the RCA and LAD coronary artery to be lower than that of the LCX coronary artery, the FFR > 0.8 for all branches, which indicates that there is no risk of myocardial infarction. The clinical manifestations of the patient during CCTA also confirm that the blood supply of the entire myocardium is adequate. (2) The FFR of each branch is analyzed separately: FFR > 0.8 for the LCX and LAD coronary arteries (slightly higher than 0.8) at all stages of operation, but for the RCA, the FFR drops significantly and is less than 0.8 during the anhepatic phase. These ischemic FFR values explain why the patient suffered a myocardial infarction during the anhepatic phase. (3) The results show that even if the patient is not diagnosed with coro-

Table 2: FFR values for each coronary artery branch obtained by numerical simulation for each stage of liver transplant surgery.

Stage	$M_1:DOFs=5.81\times10^6$			$M_2:DOFs=1.22\times10^7$		
	LAD	LCX	RCA	LAD	LCX	RCA
CCTA Scan	0.841	0.936	0.809	0.855	0.935	0.826
Anesthesia MHR	0.852	0.939	0.822	0.861	0.941	0.834
Anhepatic Phase	0.809	0.925	0.771	0.822	0.924	0.789

nary artery disease due to only a few mild stenoses, fluctuations in hemodynamics can cause myocardial ischemia, which can cause myocardial infarction in severe cases. (4) This phenomenon is in line with the clinical perspective; that is, mild stenosis of multiple vessels can be associated with postoperative hemodynamic instability and increased mortality [3].

Compared with the single-point FFR measured by the clinical pressure wire, the nu-
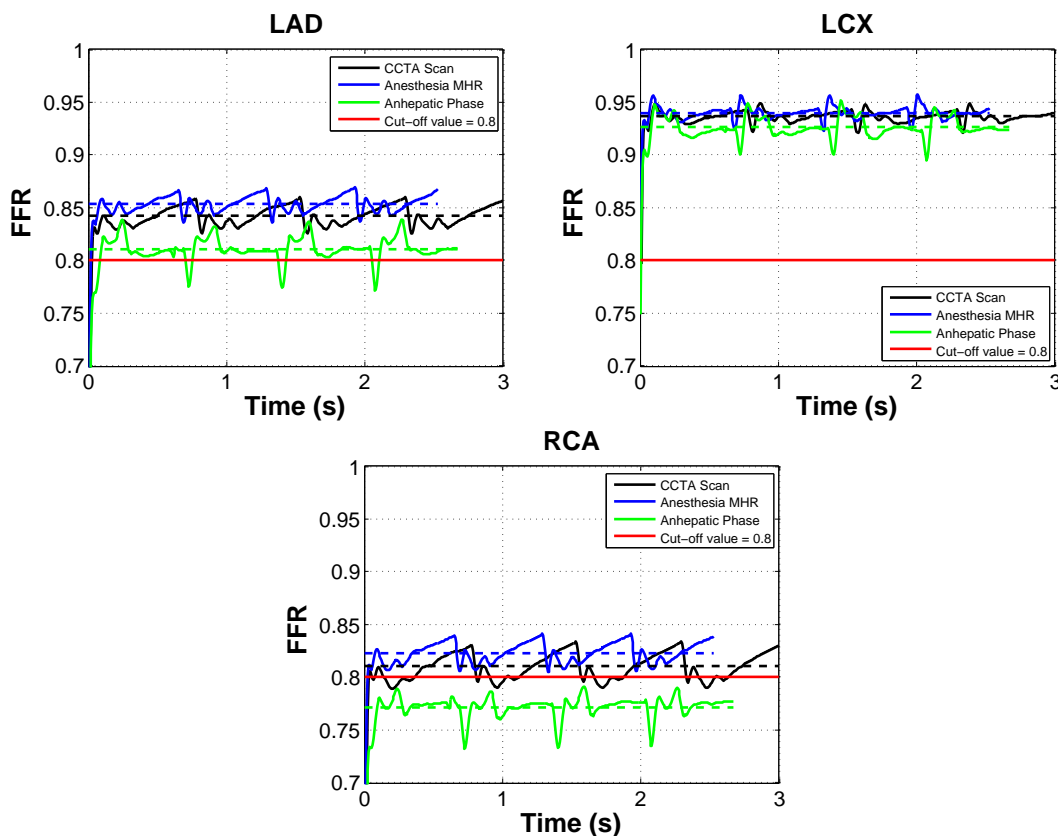

Figure 7: FFR history at the three monitoring points during different stages of the LT procedure.
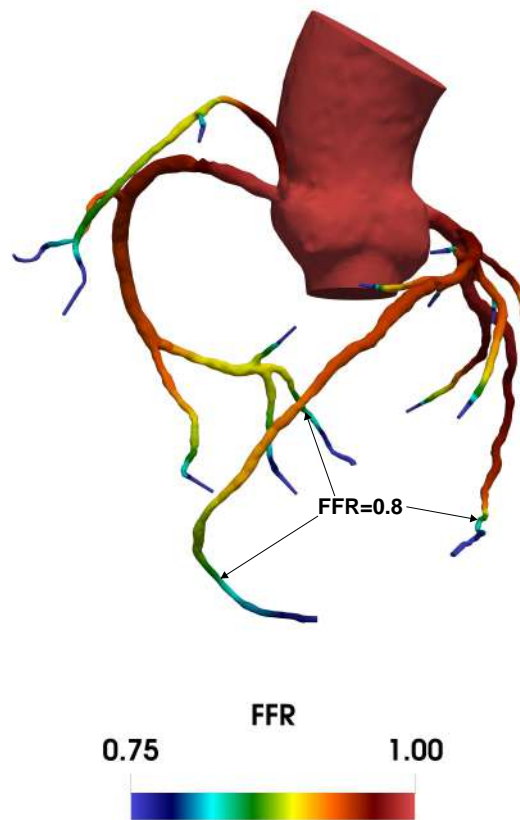
Figure 8: Simulated FFR distributions at Anhepatic phase.

merical simulation can obtain the FFR distribution of the entire coronary tree, as shown in Fig. 8, with which we can find all the possibly unhealthy arteries at Anhepatic phase.

3.2 Parallel performance

Simulation time is very important in clinical applications. A parallel scalable solver is able to reduce the simulation time by increasing the number of processors used in the simulation. In this section, we investigate the parallel performance of the proposed solver. Based on the simulation of the CCTA scan stage, the strong scalability results of the proposed solver are reported in Table 3. As shown in the table, the solver scales up to 3840 processors for the two grids M_2 and M_2. The parallel efficiency decreases with the increase of the number of processors, and with the same number of processors, the parallel efficiency for solving M_2, which has larger loads per processor, is higher than that of M_1. The reason is that the proportion of the interprocessor communication and subdomain solving time of the large mesh M_2 is smaller than that of the small mesh M_1,

Table 3: Strong scaling results of the solver. "n_p" is the number of processors, "NI" and "LI" denote the average number of nonlinear iterations per time step and the average number of GMRES iterations per Newton step, respectively. "Time" is the average total computation time in seconds per time step, "Ideal" is the ideal speedup, and "Eff" is the parallel efficiency.

n_p	$M_1: DOFs = 5.81 \times 10^6$				$M_2: DOFs = 1.22 \times 10^7$			
	NI	LI	Time	Eff	NI	LI	Time	Eff
240	3.8	346.8	129.1	100.0%	3.8	410.1	331.9	100.0%
480	3.8	348.6	73.9	87.3%	3.8	434.4	161.7	102.7%
960	3.7	388.6	42.0	76.9%	3.8	462.1	96.0	86.4%
1920	3.7	426.9	27.5	58.7%	3.8	512.1	59.6	69.6%
3840	3.7	512.0	21.1	38.3%	3.8	558.9	37.5	55.4%

and the interprocessor communication is the main factor that influences the parallel efficiency. More intuitively, the scalability results are reported in Fig. 9, where the results show that an almost linear speedup is obtained for the proposed solver. Based on the results of $n_p = 240$, the table shows that for the case M_2, the proposed solver performs with over 55% parallel efficiency when the number of processors reaches 3840.

4 Conclusions

Myocardial infarction is the main coronary artery disease affecting liver transplants. Therefore, aggressive pre-LT ischemic evaluation is necessary to assess cardiac function and identify clinically significant cardiovascular disease. However, the current gold-standard indicator, fractional flow reserve, which is based on invasive techniques, is contraindicated for most liver transplant candidates. This paper introduces a scalable CFD-based method to obtain the FFR noninvasively. A real case, which was diagnosed with several mild coronary stenoses by CCTA scan but experienced acute myocardial infarction during liver transplant, was used to evaluate the detailed hemodynamics and parallel performance of the solver.

The numerical results show that even if there is no obstructive ($\leq 50\%$) coronary stenosis by the CCTA examination, the coronary FFR could drop below 0.8, which is a reliable cut-off for hemodynamic-relevant stenoses, due to hemodynamic fluctuations after anesthesia during liver transplantation and could cause myocardial ischemia. Abnormal cardiac indicators are observed during LT, and this state is underestimated with current clinical diagnostic tools. In this case, the simulated FFR indicated that ischemia occurred in the anhepatic phase, and the FFR of the coronary artery branches with mild stenosis, LAD coronary artery and RCA in this case, decreased more than that of the branches with normal vessel anatomy.

Two scales of the problem, with 6.99×10^6 and 1.47×10^7 tetrahedral cells, are used to evaluate the parallel performance of the Newton-Krylov-Schwarz-based solver with up to 3840 processors. The results verified that the parallel efficiency is over 55% when the
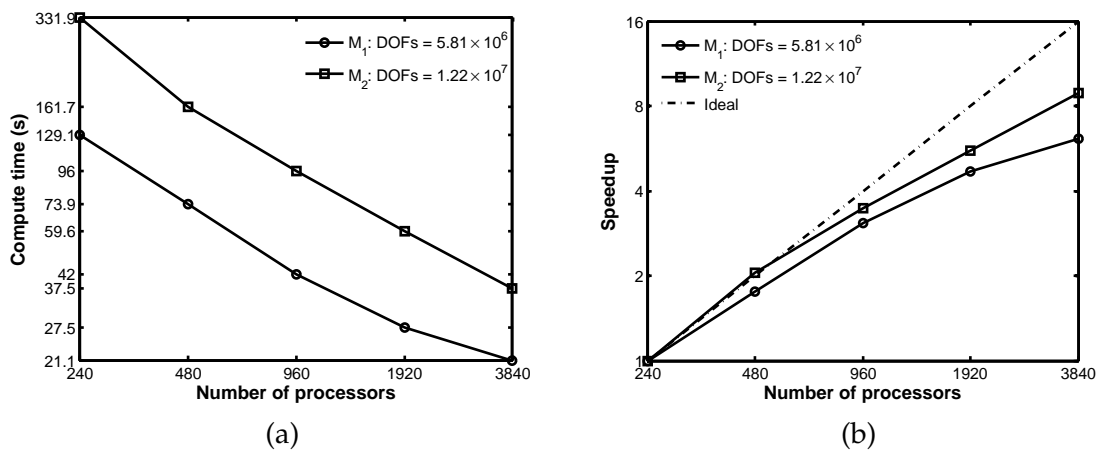
Figure 9: The average total computation time per timestep (a) and the speedup (b).

number of processors reaches 3840, the average simulation times per time step is reduced to approximately 20 seconds, and the total simulation time can be concluded in 1 hour if one cardiac cycle is considered.

5 Limitations

Although many studies have indicated the presence of an abnormal heart response during liver transplantation, its definition, prevalence, and clinical significance are unknown. Related numerical research is almost nonexistent. Thus, as a pilot study, this work has many limitations. According to the framework of the simulation and the clinical characteristics, we list some of the shortcomings below:

Clinical perspective: (1) Since numerical FFR research so far has only been performed with stable CAD patients. For the nonacute or nonserious diseases such as LT cases, its accuracy in patients with acute complicated coronary syndrome remains unknown. Numerous prospective studies in the LT patient population will significantly increase the body of available data regarding the integration of noninvasive FFR measurements into clinical decision-making. (2) More clinical monitoring data, such as real-time aortic blood flow velocity and continuous pressure monitoring, are required to model the boundary condition better for verification.

Numerical perspective: (1) The computational domain is the reconstructed geometry based on the CCTA image data, and therefore, image noise, artifacts from calcifications and motion, segmentation parameters and doctor experience can influence the accuracy of the reconstructed vascular morphology; (2) The turbulence model, non-Newtonian assumptions, and fluid-structure interactions need to be considered further to understand the blood flow motion in greater depth; and (3) To improve the algorithm's parallel per-

formance, some multilevel techniques need be applied to the blood flow simulation to insure the scalability for large number of processors.

Despite the limitations, this work is, to the authors' best knowledge, the first attempt to use the noninvasive hemodynamic gold-standard indicator FFR to assess the risk of myocardial ischemia during liver transplantation. Subsequent improvements through image segmentation, vascular geometry reconstruction, boundary conditions based on clinical data, and prospective clinical trials with a large number of cases may provide valuable reference for rapid and accurate noninvasive risk assessment in real clinical applications.

Abbreviations

BPM	beat per minute;
CAD	coronary artery disease;
CCTA	coronary computed tomography angiography;
CFD	computational fluid dynamics;
CVD	cardiovascular disease;
DOFs	degrees of freedom;
EF	ejection fraction;
FFR	fractional flow reserve;
LAD	left anterior descending;
LCX	left circumflex;
LT	liver transplantation;
MHR	maximum heart rate;
NKS	Newton-Krylov-Schwarz;
RAS	restricted additive Schwarz;
RCA	right coronary artery;
SBP and **DBP**	systolic and diastolic blood pressure;
SV	stroke volume;
MI	myocardial infarction.

Acknowledgements

References

[1] M. L. VOLK, J. C. HERNANDEZ, A. S. LOK, AND J. A. MARRERO, *Modified Charlson co-morbidity index for predicting survival after liver transplantation,* Liver Transplantation, 13(11) (2007), pp. 1515–1520.

[2] L. B. VANWAGNER, B. LAPIN, J. LEVITSKY, J. T. WILKINS, M. M. ABECASSIS, A. I. SKARO, AND D. M. LLOYD-JONES, *High early cardiovascular mortality after liver transplantation,* Liver Transplantation, 20(11) (2014), pp. 1306–1316.

[3] L. B. VANWAGNER, M. E. HARINSTEIN, J. R. RUNO, C. DARLING, M. SERPER, S. HALL, J. A. KOBASHIGAWA, AND L. L. HAMMEL, *Multidisciplinary approach to cardiac and pulmonary vascular disease risk assessment in liver transplantation: an evaluation of the evidence and consensus recommendations,* American J. Transplantation, 18(1) (2018), pp. 30–42.

[4] S. S. PATEL, E. NABI, L. GUZMAN, A. ABBATE, C. BHATI, R. T. STRAVITZ, T. REICHMAN, S. C. MATHERLY, C. DRISCOLL, H. LEE, V. A. LUKETIC, R. K. STERLING, A. J. SANYAL, V. PATEL, M. LEVY, AND M. S. SIDDIQUI, *Coronary artery disease in decompensated patients undergoing liver transplantation evaluation,* Liver Transplantation, 24(3) (2018), pp. 333–342.

[5] S. ALEXANDER, M. TESHOME, H. PATEL, E. Y. CHAN, AND R. DOUKKY, *The diagnostic and prognostic utility of risk factors defined by the AHA/ACCF on the evaluation of cardiac disease in liver transplantation candidates,* BMC Cardiovascular Disorders, 19(1) (2019), pp. 1–6.

[6] S. D. KRISTENSEN, J. KNUUTI, A. SARASTE, S. ANKER, H. E. BØTKER, S. D. HERT, I. FORD, J. R. GONZALEZ-JUANATEY, B. GORENEK, G. R. HEYNDRICKX, A. HOEFT, K. HUBER, B. IUNG, K. P. KJELDSEN, D. LONGROIS, T. F. LÜSCHER, L. PIERARD, S. POCOCK, S. PRICE, AND M. ROFFI, *Authors/task force members, 2014 ESC/ESA Guidelines on non-cardiac surgery: cardiovascular assessment and management: The joint task force on non-cardiac surgery: cardiovascular assessment and management of the European Society of Cardiology (ESC) and the European Society of Anaesthesiology (ESA),* Euro. Heart J., 35(35) (2014), pp. 2383–2431.

[7] L. A. FLEISHER, K. E. FLEISCHMANN, A. D. AUERBACH, S. A. BARNASON, J. A. BECK-MAN, B. BOZKURT, V. G. DAVILA-ROMAN, M. D. GERHARD-HERMAN, T. A. HOLLY, G. C. KANE, J. E. MARINE, M. T. NELSON, C. C. SPENCER, A. THOMPSON, H. H. TING, B. F. URETSKY, AND D. N. WIJEYSUNDERA, *2014 ACC/AHA guideline on perioperative cardiovascular evaluation and management of patients undergoing noncardiac surgery: a report of the American College of Cardiology/American Heart Association Task Force on Practice Guidelines,* Circulation, 130(24) (2014), pp. e278–e333.

[8] S. S. PATEL, F. P. LIN, V. A. RODRIGUEZ, C. BHATI, B. V. JOHN, T. PENCE, M. B. SIDDIQUI, A. P. SIMA, A. ABBATE, T. REICHMAN, AND M. S. SIDDIQUI, *The relationship between coronary artery disease and cardiovascular events early after liver transplantation,* Liver International, 39(7) (2019), pp. 1363–1371.

[9] J. M. MILLER, C. E. ROCHITTE, M. DEWEY, A. ARBAB-ZADEH, H. NIINUMA, I. GOTTLIEB, N. PAUL, M. E. CLOUSE, E. P. SHAPIRO, J. HOE, A. C. LARDO, D. E. BUSH, A. DE ROOS, C. COX, J. BRINKER, AND J. A. LIMA, *Diagnostic performance of coronary angiography by 64-row CT,* The New England J. Medicine, 359(22) (2008), pp. 2324–2336.

[10] W. B. MEIJBOOM, M. F. MEIJS, J. D. SCHUIJF, M. J. CRAMER, N. R. MOLLET, C. A. VAN MIEGHEM, K. NIEMAN, J. M. VAN WERKHOVEN, G. PUNDZIUTE, A. C. WEUSTINK, A. M. DE VOS, F. PUGLIESE, B. RENSING, J. W. JUKEMA, J. J. BAX, M. PROKOP, P. A. DO-EVENDANS, K. G. HUNINK, G. P. KRESTIN, AND P. J. DE FEYTER, *Diagnostic accuracy of 64-slice computed tomography coronary angiography: a prospective, multicenter, multivendor study,* J. American College of Cardiology, 52(25) (2008), pp. 2135–2144.

[11] N. H. PIJLS, J. A. VAN SON, R. L. KIRKEEIDE, B. L. G. K. DE BRUYNE, AND K. L. GOULD, *Experimental basis of determining maximum coronary, myocardial, and collateral blood flow by pressure measurements for assessing functional stenosis severity before and after percutaneous transluminal coronary angioplasty,* Circulation, 87(4) (1993), pp. 1354–1367.

[12] N. H. PIJLS, B. VAN GELDER, P. VAN DER VOORT, K. PEELS, F. A. BRACKE, H. J. BONNIER, AND M. I. EL GAMAL, *Fractional flow reserve: a useful index to evaluate the influence of an epicardial coronary stenosis on myocardial blood flow,* Circulation, 92(11) (1995), pp. 3183–3193.

[13] Y. KIM, Y. PARK, AND S. LIM, *3D simulations of blood flow dynamics in compliant vessels: normal, aneurysmal, and stenotic arteries,* Commun. Comput. Phys., 19 (2016), pp. 1167–1190.

[14] K. ZHOU, AND Y. SHANG, *A parallel pressure projection stabilized finite element method for stokes equation with nonlinear slip boundary conditions,* Adv. Appl. Math. Mech., 12 (2020), pp. 1438–1456.

[15] Y. LUO, H. LI, S. HAN AND S. ZHANG, *Direct numerical simulations of self-sustained oscillations in two-dimensional open cavity for subsonic and supersonic flow,* Adv. Appl. Math. Mech., 13 (2021), pp. 942–965.

[16] S. YANG, Y. LIU, H. LIU, AND C. WANG, *Numerical methods for semilinear fractional diffusion equations with time delay,* Adv. Appl. Math. Mech., 14 (2022), pp. 56–78.

[17] I. KESLER, R. LAN, AND P. SUN, *The arbitrary Lagrangian-Eulerian finite element method for a transient Stokes/parabolic interface problem,* Int. J. Numer. Anal. Model., 18 (2021), pp. 339–361.

[18] C. A. TAYLOR, T. A. FONTE, AND J. K. MIN, *Computational fluid dynamics applied to cardiac computed tomography for noninvasive quantification of fractional flow reserve: scientific basis,* J. American College of Cardiology, 61(22) (2013), pp. 2233–2241.

[19] B. L. NØRGAARD, J. LEIPSIC, S. GAUR, S. SENEVIRATNE, B. S. KO, H. ITO, J. M. JENSEN, L. MAURI, B. DE BRUYNE, H. BEZERRA, AND K. OSAWA, *Diagnostic performance of noninvasive fractional flow reserve derived from coronary computed tomography angiography in suspected coronary artery disease: the NXT trial (Analysis of Coronary Blood Flow Using CT Angiography: Next Steps),* J. American College of Cardiology, 63(12) (2014), pp. 1145–1155.

[20] M. LI, J. LI, R. MARTIN, AND K. ZHANG, *A numerical framework to simplify CAD models for reliable estimates of physical quantities,* Adv. Appl. Math. Mech., 11(4) (2019), pp. 870–889.

[21] H. M. KWON, AND G. S. HWANG, *Cardiovascular dysfunction and liver transplantation,* Korean J. Anesthesiology, 71(2) (2018), pp. 85–91.

[22] P. SEGERS, N. STERGIOPULOS, N. WESTERHOF, P. WOUTERS, P. KOLH, AND P. VERDONCK, *Systemic and pulmonary hemodynamics assessed with a lumped-parameter heart-arterial interaction model,* J. Eng. Math., 47(3) (2003), pp. 185–199.

[23] I. E. VIGNON-CLEMENTEL, C. A. FIGUEROA, K. E. JANSEN, AND C. A. TAYLOR, *Outflow boundary conditions for 3D simulations of non-periodic blood flow and pressure fields in deformable arteries,* Comput. Methods Biomech. Biomed. Eng., 13(5) (2010), pp. 625–640.

[24] M. S. OLUFSEN, A. NADIM, AND L. A. LIPSITZ, *Dynamics of cerebral blood flow regulation explained using a lumped parameter model,* American J. Physiology-Regulatory, Integrative and Comparative Physiology, 282(2) (2002), pp. R611–R622.

[25] E. MEANEY, F. ALVA, R. MOGUEL, A. MEANEY, J. ALVA, AND R. WEBEL, *Formula and nomogram for the sphygmomanometric calculation of the mean arterial pressure,* Heart, 84(1) (2000), pp. 64–64.

[26] P. J. BLANCO, S. M. WATANABE, E. A. DARI, M. A. R. PASSOS, AND R. A. FEIJÓO, *Blood flow distribution in an anatomically detailed arterial network model: criteria and algorithms,* Biomech. Model. Mechanobiology, 13(6) (2014), pp. 1303–1330.

[27] R. L. SANI, P. M. GRESHO, R. L. LEE, AND D. F. GRIFFITHS, *The cause and cure of the spurious*

pressures generated by certain FEM solutions of the incompressible Navier-Stokes equations: Part 1, Int. J. Numer. Methods Fluids, 1(1) (1981), pp. 17–43.

[28] L. P. FRANCA, AND S. L. FREY, *Stabilized finite element methods: II. The incompressible Navier-Stokes equations,* Comput. Methods Appl. Mech. Eng., 99(2-3) (1992), pp. 209–233.

[29] U. M. ASCHER, AND L. R. PETZOLD, Computer Methods for Ordinary Differential Equations and Differential-Algebraic Equations, SIAM, 1998.

[30] S. S. RAVINDRAN, *Analysis of a second-order decoupled time-stepping scheme for transient viscoelastic flow,* Int. J. Numer. Anal. Model., 17(1) (2020), pp. 87–109.

[31] X. C. CAI, AND M. SARKIS, *A restricted additive Schwarz preconditioner for general sparse linear systems,* SIAM J. Sci. Comput., 21(2) (1999), pp. 792–797.

[32] R. CHEN, Y. WU, Z. YAN, Y. ZHAO, AND X. C. CAI, *A parallel domain decomposition method for 3D unsteady incompressible flows at high Reynolds number,* J. Sci. Comput., 58(2) (2014), pp. 275–289.

[33] Z. YAN, R. CHEN, Y. ZHAO, AND X. C. CAI, *Numerical aerodynamic simulation of transient flows around car based on parallel Newton-Krylov-Schwarz algorithm,* Appl. Anal., 100(7) (2021), pp. 1501–1513.

[34] X. C. CAI, M. DRYJA, AND M. SARKIS, *Restricted additive Schwarz preconditioners with harmonic overlap for symmetric positive definite linear systems,* SIAM J. Numer. Anal., 41(4) (2003), pp. 1209–1231.

[35] S. BALAY, S. ABHYANKAR, M. F. ADAMS, J. BROWN, P. BRUNE, K. BUSCHELMAN, L. DALCIN, A. DENER, A. EIJKHOUT, W. D. GROPP, D. KARPEYEV, D. KAUSHIK, M. G. KNEPLEY, D. A. MAY, L. C. MCINNES, R. T. MILLS, T. MUNSON, K. RUPP, P. SANAN, B. F. SMITH, S. ZAMPINI, H. ZHANG, AND H. ZHANG, *PETSc Web page,* `https://www.mcs.anl.gov/petsc` (2019).

[36] ANSYS Inc., ICEM CFD User's manual, Release 19.2 (2018).

[37] G. KARYPIS, AND V. KUMAR, ParMETIS–parallel graph partitioning and fill-reducing matrix ordering, version 4, `http://www.cs.umn.edu/~metis`, (2014).

[38] U. AYACHIT, The ParaView Guide: A Parallel Visualization Application, Kitware, Inc., Clifton Park, NY, USA, 2015.

[39] G. N. LEVINE, E. R. BATES, J. C. BLANKENSHIP, S. R. BAILEY, J. A. BITTL, B. CERCEK, C. E. CHAMBERS, S. G. ELLIS, R. A. GUYTON, S. M. HOLLENBERG, U. N. KHOT, R. A. LANGE, L. MAURI, R. MEHRAN, I. D. MOUSSA, D. MUKHERJEE, B. K. NALLAMOTHU, AND H. H. TING, *2011 ACCF/AHA/SCAI Guideline for Percutaneous Coronary Intervention. A report of the American College of Cardiology Foundation/American Heart Association Task Force on Practice Guidelines and the Society for Cardiovascular Angiography and Interventions,* J. American College of Cardiology, 58(24) (2011), pp. e44–e122.